



# Graphene oxide aerogels for adsorptive separation of aromatic hydrocarbons and cycloalkanes

Maksymilian Plata-Gryl<sup>a,\*</sup>, Roberto Castro-Muñoz<sup>a</sup>, Emilia Gontarek-Castro<sup>b</sup>, Alan Miralrio<sup>c</sup>, Grzegorz Boczkaj<sup>a,d</sup>

<sup>a</sup> Department of Sanitary Engineering, Faculty of Civil and Environmental Engineering, Gdansk University of Technology, Narutowicza Str. 11/12, Gdansk 80-233, Poland

<sup>b</sup> Department of Environmental Technology, Faculty of Chemistry, University of Gdansk, Wita Stwosza Str. 63, 80-308 Gdansk, Poland

<sup>c</sup> Tecnológico de Monterrey, Escuela de Ingeniería y Ciencias, Ave. Eugenio Garza Sada 2501, Monterrey, N.L., 64849, Mexico

<sup>d</sup> Advanced Materials Centre, Gdansk University of Technology, Narutowicza Str. 11/12, Gdansk 80-233, Poland

## ARTICLE INFO

### Keywords:

Benzene  
Cyclohexane  
Nanomaterials  
Reduced graphene oxide aerogels  
Adsorption  
Separation

## ABSTRACT

Efficient separation of benzene and cyclohexane has critical importance for production of commodity chemicals, and is one of the most challenging separations in the industry. Physisorption by recyclable, porous solids has a significant potential in substituting energy-intensive azeotropic or extractive distillation methods. Reduced graphene oxide aerogels (rGOAs) are emerging materials holding great promise for connecting unique properties of 2D graphene with ordinary 3D materials. The benzene/cyclohexane separation on rGOAs self-assembled by the chemical reduction with *l*-ascorbic acid, sodium bisulphite and (for the first time) sodium dithionite was studied by dynamic gas adsorption methods, and the adsorption performance was analysed in relation to aerogels physicochemical properties. The aerogel reduced with sodium dithionite (rGOA\_DTN) had the highest reduction degree and specific surface area (461.2 m<sup>2</sup>g<sup>-1</sup>), with the highest contribution of mesopores. It was also the sample with the uppermost uptake of benzene and cyclohexane. The binary component adsorption on rGOA\_DTN resulted in the selectivity of the adsorption of benzene over cyclohexane of 2.1. Adsorption-desorption studies demonstrated the excellent thermal stability of the adsorbent in the long-run operation. Because the adsorption capacity did not correlate with the mesopores but with macropores surface area, the selectivity of the adsorption was attributed to the different physicochemical structure of aerogels surface. The benzene molecule interacted strongly by specific C-H... $\pi$  interactions, while the cyclohexane molecule was excluded from the surface of aerogels because of its shape/size. Results demonstrated that rGOAs can be a versatile and flexible platform for adsorptive gas-phase hydrocarbons separation.

## 1. Introduction

Efficient separation of hydrocarbons is essential to the chemical and material processing industries. The example of important but problematic separation is the removal of benzene from cyclohexane – an important intermediate for production of thermoplastic polyamide-based polymers, *i.e.*, Nylon 6 and Nylon 66, obtained mainly by catalytic hydrogenation of benzene [1,2]. Moreover, removal of benzene is dictated not only by the quality of the final product but also by environmental and legislative limitations as it is recognized for carcinogenicity and mutagenicity [3]. The challenge of this separation lies in close

boiling point values of benzene (80.1 °C) and cyclohexane (80.7 °C), similar chemical structure and formation of azeotrope. Table 1 presents the properties of both compounds. Moreover, depending on the application, high purity of the separated compounds may be required, which further complicates the separation process and increases the overall cost. This demands the use of complex and energy-intensive extractive distillation, azeotropic distillation or pervaporative separation methods [4–6]. Thus, the development of new technologies is needed to improve both the efficiency, simplicity and sustainability of the benzene and cyclohexane separation processes.

Alternative is sought in the adsorption technique as porous materials

\* Corresponding author at: Department of Sanitary Engineering, Faculty of Civil and Environmental Engineering, Gdansk University of Technology, Narutowicza Str. 11/12, Gdansk 80-233, Poland.

E-mail address: [maksymilian.plata-gryl@pg.edu.pl](mailto:maksymilian.plata-gryl@pg.edu.pl) (M. Plata-Gryl).

<https://doi.org/10.1016/j.cej.2024.152782>

Received 8 April 2024; Received in revised form 22 May 2024; Accepted 1 June 2024

Available online 2 June 2024

1385-8947/© 2024 The Authors. Published by Elsevier B.V. This is an open access article under the CC BY-NC-ND license (<http://creativecommons.org/licenses/by-nc-nd/4.0/>).

**Table 1**

Physical and chemical properties of cyclohexane and benzene. Data extracted from [7–9].

	Cyclohexane	Benzene
Molecular formula	C <sub>6</sub> H <sub>12</sub>	C <sub>6</sub> H <sub>6</sub>
Molecular weight / g/mol	84.16	78.11
Boiling point / K	353.9	353.3
Dipole moment / D	0.0	0.0
L-J potential / Å	6.182	5.349
Kinetic diameter / Å	6.00	5.85
Critical diameter / Å	6.90	6.63
* $\Delta_{\text{vap}}H(453.15 \text{ K}) / \text{kJ/mol}$	23.59	22.68
Polarizability / Å <sup>3</sup>	11.000	10.330

\* The  $\Delta_{\text{vap}}H$  was calculated for the experimental temperature (453.15 K) with equation described in [7].

(adsorbents) can discriminate molecules with minor structural differences. The separation can be driven by differences in molecular size or/and intermolecular interactions with adsorbents surface. Kinetic selectivity originates from diffusion barriers created by pores of different dimensions and is dominant in adsorbents devoid of specific adsorption centres that can form thermodynamically stable and relatively lasting complexes with adsorbate. Such mechanism of benzene and cyclohexane separation is preeminent in micro-mesoporous silicas [10] and carbons [11,12]. These adsorbents typically have high surface areas, which provides ample sites for adsorption but don't automatically result in efficient separation. For ordered mesoporous carbons (OMC), high adsorption amounts were achieved for both benzene and cyclohexane because pore size was large enough to be accessed by both type of molecules. It made it a potential adsorbent for disposal of these compounds but not for selective separation [11]. Better separation was obtained with microporous carbons where selectivity was a product of the micropore volume and chemistry of the surface. Smaller pore size of the activated carbons helped to achieve differentiation in diffusion rates among benzene and cyclohexane and the unique surface physicochemical structure determined interactions with adsorbates [12].

Selectivity enhancement by tailoring pore dimensions is the main area of interest in selective separations by metal–organic frameworks (MOFs) [1,13]. Incorporation of pores with precisely selected dimensions, can allow MOFs to selectively exclude bulkier cyclohexane molecules (kinetic diameter of 6 Å compared to 5.85 Å for benzene [14,15]). Additionally, chemistry of apertures can be contoured to enhance adsorption affinity and selectivity [13], and even reverse selectivity – promote adsorption of cyclohexane over benzene [14]. Preferential uptake of cyclohexane was also observed in thienothiophene cages as a result of strong hydrogen bonding between cyclohexane and thienothiophene ligand [16] and in spatially confined carborane metallcage where a dihydrogen bonding was responsible for high selectivity toward cyclohexane [17].

Although cyclohexane and benzene molecules are both poorly polar, the delocalized  $\pi$ -electron cloud in benzene result in uneven distribution of electrostatic potential and give a chance for formation of specific adsorbate-adsorbent interactions and enhancement of molecular recognition. Considering that both compounds are stable species, the additional stabilization of benzene is commonly explained by its aromatic nature. The above due to its six  $\pi$  electrons, fulfilling the widely accepted Hückel  $4n + 2$  rule [18], as well as alternative approaches such as the anisotropy of the current-induced density [19]. The study of the  $\pi$ -cation interaction has gained relevance within the scientific community as a key force influencing molecular recognition [20] and ion trapping capabilities [21]. In zeolites, such interactions occur when benzene  $\pi$ -electron cloud is attracted by a cation of a zeolite [22]. Nonporous amide naphthotubes exhibit excellent separation efficiency of benzene due to N-H... $\pi$  interactions between amide group and benzene  $\pi$ -electrons [23]. The  $\pi$ -type interactions play a crucial role in the selective uptake of benzene in adsorbents with aromatic structures

within their frameworks, such as triptycene-based cyanate resins [24,25] or imine-linked covalent organic frameworks where the uptake of benzene was additionally enhanced by guest-induced plasticity of pores [26]. In MOFs, it was observed that a higher degree of  $\pi$ -conjugation within their structure significantly increases benzene uptake [1]. Furthermore, the decoration of a framework with functional groups like  $-\text{NO}_2$  can strengthen interaction with benzene [15], or even reverse selectivity, as observed in MOFs modified with amino groups, which preferentially uptake cyclohexane [27]. The strong affinity of  $-\text{NO}_2$  groups for benzene was also reported for other adsorbents [28,29].

An emerging group of materials with a high degree of  $\pi$ -conjugation are reduced graphene oxide aerogels (rGOA), which are obtained by the reduction induced self-assembly of graphene oxide (GO). Fig. 1 illustrates the process of rGOA formation. The reduction of oxygen containing groups of GO, which are normally responsible for repulsion between them and good stability of GO dispersion, increases the hydrophobic and electrostatic attraction, as well as  $\pi$ - $\pi$  stacking, resulting in self-assembly of a porous 3D network. Finally, the water is removed by the freeze-drying or supercritical CO<sub>2</sub> drying. The reduction can be accomplished in hydrothermal conditions or with the aid of chemical reductant in moderate temperatures (below 100 °C). A variety of substances can be used as chemical reductants, including *l*-ascorbic acid [30], ethylenediamine [31], sodium bisulphite [32], urea [33] or even soft drinks [34]. Depending on their nature, some of reductants can additionally modify the structure of rGOA by doping it with heteroatoms [35], providing additional crosslinking [36] or introducing functional groups [34].

The goal of the rGOA assembly is to connect unique 2D properties of rGO with the ordinary, practical 3D materials. Aerogels based on rGO are anticipated as technology enhancing materials in catalysis [37], semi-conducting devices, sensors [38], energy-related applications [32] or adsorption at both gas–solid [39] and liquid–solid [40] interface. Especially in adsorption, the highly interconnected porous structure and  $\pi$ -electron-rich surface can be of high importance for adsorption performance. Recently, rGOAs were tested for adsorption of benzene, toluene and xylene isomers [39] or hexamethyldisioxane [41] from gas phase, and the significant uptake of adsorbates was attributed mainly to the high surface area of rGOAs. The high surface area was also essential for phenol gas sensing performance in rGOA based sensors. Moreover, such sensors demonstrated selectivity for different aromatic hydrocarbons [42]. Nevertheless, the application of rGOAs in gas-phase adsorption is still in its infancy and requires extensive research in the near future, specially, to identify caveats for successful implementation. At the moment, the most significant limitations are the mechanical strength [39] and macro-mesoporous texture (from the point of view selective adsorption) of rGOAs.

Textural structure of rGOAs is usually described by type II isotherms with H3 hysteresis loop characteristic for meso-macroporous materials [43]. The surface area of rGOA can range between tens to few hundreds of m<sup>2</sup>/g [39,41,43]. If freeze-drying is used for hydrogel drying, it is possible to adjust the porous structure by controlling the ice formation. This can be achieved, for example, through directional freezing [44] or temperature adjustment [45], to limit the accessibility of pores to molecules with certain shape and size. Recent studies have also revealed that molecules can be excluded from the interaction with the surface of rGOA because of its nanoroughness [45]. Thus, even if two molecules will access the same pores, the bulkier one (e.g. more branched) can be restricted from interacting with the surface. If the interaction occurs between rGOA and adsorbate, the surface of rGO gives an opportunity for different types of surface interactions including: van der Waals, hydrophobic,  $\pi$ - $\pi$ , electrostatic, hydrogen bonds or ion- $\pi$  interaction [46]. Fig. 2 shows the types of possible intermolecular interactions of rGO/GO/graphene. The structure of rGO/GO/graphene, *i.e.*, defects and oxygen containing functional groups, will largely dictate surface interactions with molecules.

Aerogels self-assembled from rGO meet all the requisites for being an

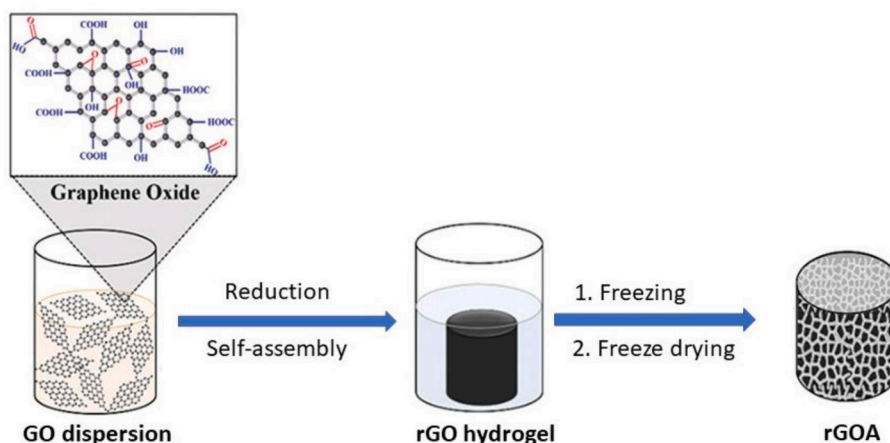


Fig. 1. Schematic illustration of rGOA synthesis process from GO by reduction induced self-assembly.

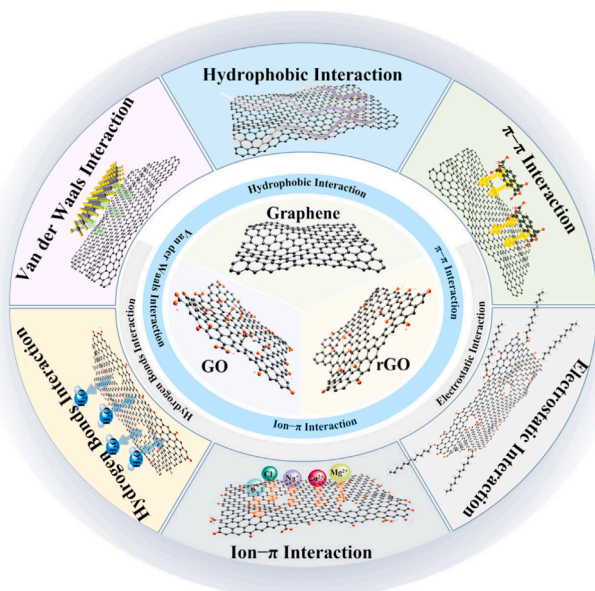


Fig. 2. Non-covalent intermolecular interactions of GO/rGO/graphene. Reprinted with permission from [46].

excellent adsorbent for gas-phase selective separations. In this work, three types of rGOAs were synthesized through reduction induced self-assembly and freeze-drying using different reductants, namely: *l*-ascorbic acid, sodium bisulphite, and sodium dithionite. The effect of reductant type on the physicochemical structure and adsorptive separation of hydrocarbons with similar size and intermolecular interactions was analysed. The potential for such application was demonstrated in our previous work, in which aerogels reduced with *l*-ascorbic acid exhibited capacity for selective adsorption of organic compounds based on kinetic and thermodynamic effects [45]. Herein, we further explore this topic using the challenging benzene/cyclohexane separation as a model example. To the best of our knowledge, it is the first time that rGOAs synthesized with different reductants were used for such separation.

## 2. Methods

### 2.1. Graphene oxide (GO) synthesis

GO was obtained by the Tour's method [47]. That is, a 1 g of

synthetic graphite powder (7–11  $\mu\text{m}$ , 99 %, Alfa Aesar) was mixed with 120 mL sulfuric acid (min.95 %, pure p.a., POCH, Poland) and 15 mL of *ortho*-phosphoric acid (85 %, pure p.a.-basic, POCH, Poland). Next, 6 g of  $\text{KMnO}_4$  (pure p.a., POCH, Poland) was added in small doses to avoid overheating and keep the temperature of the mixture below 20  $^\circ\text{C}$ . After addition of all  $\text{KMnO}_4$ , the mixture was heated for 12 h at 50  $^\circ\text{C}$  with mixing, using MS-H-Pro<sup>T</sup> magnetic hot plate stirrer (Chemland, Poland). Then, it was cooled to room temperature and oxidation was stopped by addition of 250 mL of cold ultrapure water (ultrapure Type 1 from Direct-Q® 3UV-R system, Merck Millipore, Germany) and 3 mL of  $\text{H}_2\text{O}_2$  (30 %, pure p.a., POCH, Poland). The oxidized graphite was additionally washed with ultrapure water, until the pH of the supernatant was neutral. The water was removed by evaporation under reduced pressure (20 mbar) at 30  $^\circ\text{C}$  (Rotavapor R-300, Buchi, Germany).

Graphite oxide was exfoliated with the ultrasonic probe (UP400St, Hielscher, Germany) with radiation area of 2.2  $\text{cm}^2$ . Graphite oxide mixture of 10  $\text{mg mL}^{-1}$  concentration was ultrasonicated two times for 15 min at 200 W, in a cooling bath (0  $^\circ\text{C}$ ) to avoid overheating. Obtained dispersion was left in the refrigerator (6  $^\circ\text{C}$ ) to settle out the unexfoliated graphite oxide. The suspension of exfoliated GO was concentrated with rotary evaporator and finally freeze-dried. Obtained solid GO was used for rGOA fabrication.

### 2.2. Fabrication of reduced graphene oxide aerogels (rGOA)

Aerogels samples were prepared by chemical reduction of GO to rGO hydrogel and subsequent freeze-drying. The GO dispersion (2  $\text{mg mL}^{-1}$ ) was mixed in a glass container with reductant and placed in an oven at 95  $^\circ\text{C}$  for 24 h. As reductants, *l*-ascorbic acid (LAA, pure p.a., Chempur, Poland),  $\text{NaHSO}_3$  (BS, ACS grade, Thermo Scientific, Belgium) and sodium dithionite (DTN, EMSURE®, Merck, Germany) were used in 4:1, 1:1 and 2:1 ratio to GO by mass, respectively. After reduction, black monoliths of hydrogels were obtained. To remove impurities (by-products and unreacted reductant), hydrogels were washed several times with deionized water. Finally, the hydrogels were frozen in the liquid nitrogen and water was removed by freeze-drying at a pressure below 20 Pa provided by rotary vacuum pump RV8 (Edwards, UK). The endpoint of sublimation was indicated by a Pirani-type vacuum gauge. The as-synthesized aerogels samples were labelled as rGOA\_LAA, rGOA\_BS and rGOA\_DTN (with last letters indicating the type of the reductant) and used for further tests without any modifications.

### 2.3. Fourier-transform infrared spectroscopy (FTIR)

Fourier transform infrared spectra were performed using IR-Tracer 100 spectrometer (Shimadzu, Japan) equipped with attenuated total

reflectance (ATR) accessory. Spectra were collected in the 800–3800  $\text{cm}^{-1}$  range with 2  $\text{cm}^{-1}$  resolution. Spectrum of each sample was an average of 40 scans.

#### 2.4. Raman spectroscopy

The Raman spectra were measured with a Thermo Scientific DXR Smart Raman spectrometer with a 532 nm laser as the excitation source under ambient conditions.

#### 2.5. Nitrogen adsorption

The BET (Brunauer-Emmett-Teller) surface area was determined using sorption analyzer 3P Instrument Micro 200. The sample was degassed for 5 h at 200 °C prior to measurement. Presence of micropores was assessed using the t-plot method.

#### 2.6. Inverse gas chromatography (IGC)

IGC experiments were conducted on the Autosystem XL (Perkin Elmer, USA) gas chromatograph (GC) with flame ionization detector (FID), controlled by a TotalChrom 6.3.2 software (Perkin Elmer, USA). Aerogels samples of about 20 mg were packed inside the stainless-steel columns (5 cm length, 3.62 mm i.d.) with both ends plugged with a silane-treated glass wool (50MGS, Hewlett Packard, USA). Prior to analysis, columns were conditioned in the flow of a nitrogen carrier gas (N5.0, Linde Gas, Poland) under temperature program (10 min at 323 K – 5 K  $\text{min}^{-1}$  – 180 min at 523 K). IGC experiments were performed under nitrogen flowrate of 30  $\text{mL min}^{-1}$  at a range of temperatures between 453 and 473 K. The flowrate was controlled with GFM Pro flowmeter (Thermo Scientific, USA). For calculations, it was corrected for compressibility of carrier gas and temperature of the column. Injector and detector temperatures were maintained at 523 K. The list of injected test probes included:  $\text{C}_5\text{-C}_9$  *n*-alkanes, isooctane, cyclooctane, benzene and cyclohexane. Each probe was injected at least two times and methane was used as the inert reference probe. The volume of injection was adjusted between 0.1 – 1.0  $\mu\text{L}$  with 1  $\mu\text{L}$  non-dead volume microsyringe (VWR, USA). If lower amounts of probe were required for tests, a gaseous mixture with nitrogen was prepared in a TEDLAR® bag (SKC, UK) and appropriate amount was injected with a 100  $\mu\text{L}$  gas-tight syringe (VWR, USA). Because of the high probes concentrations, the IGC runs were conducted at finite concentration conditions (IGC-FC) where relatively high surface coverages ( $\theta$ ) can be obtained. All IGC-FC calculations (desorption isotherms, morphology indices, dispersive component of the surface free energy, dispersive and specific free energies of adsorption) were made with a self-made software developed in Python programming language. All values resulting from IGC-FC calculations are reported for  $\theta = 0.01$ , unless indicated otherwise. Details of calculations can be found in Text S1.

#### 2.7. Temperature programmed desorption (TPD)

TPD data was collected with the same GC-FID instrument as in IGC experiments. Nitrogen was used as a carrier gas with flowrate of 20  $\text{mL min}^{-1}$ . The adsorbent bed was saturated with benzene or cyclohexane at 343 K by injecting 30  $\mu\text{L}$  of the probe into the column in three parts (10  $\mu\text{L}$  per injection in 10-minute periods). After that, the adsorption column was left overnight, under carrier gas flow until the signal of FID detector reached baseline. TPD was started at 323 K at different linear heating rates (2, 5, 8 K  $\text{min}^{-1}$ ) and the final temperature was 523 K. When it was reached, the desorption was continued isothermally for 60 min to desorb all reversibly adsorbed molecules. Based on the TPD peaks measured at different heating rates ( $\beta_H$ , K), the activation energy of desorption ( $E_d$ , kJ/mol) of a probe compound can be calculated according to the Polanyi-Wigner equation, as expressed below in the linearized form:

$$\ln\left(\frac{RT_p^2}{\beta_H}\right) = \frac{E_d}{R} \frac{1}{T_p} + \ln\left(\frac{E_d}{K_0}\right) \quad (1)$$

where  $T_p$  is the peak temperature on the TPD curve (K) and  $R$  is the gas constant, and  $K_0$  is the rate coefficient of desorption ( $\text{s}^{-1}$ ).

#### 2.8. Fixed-bed (dynamic) adsorption experiments

Experimental set up for dynamic adsorption was assembled in the laboratory and consisted of a gas cylinder, pressure and flow regulator, three-way valve, isothermal chamber with a stainless steel adsorption column (the same as for IGC experiments), fused silica capillary pre-column for conditioning of inlet gas at experimental temperature (15 m long, 0.320 mm i.d., deactivated), flame ionization detector (FID, Perkin Elmer, USA), analog-to-digital converter (Nelson 900, Perkin Elmer, USA) and a computer operating the TotalChrom 6.3.2 software (Perkin Elmer, USA) for acquisition of data. Experiments were conducted at 50 °C with single and binary component mixtures at a flowrate of 5  $\text{mL min}^{-1}$ . For binary component tests, the setup was additionally equipped with a manual six-way valve with injection loop (100  $\mu\text{L}$ ) and 60 m capillary column installed between adsorption column and FID, for analysis of gas composition. The concentration of benzene and cyclohexane (in nitrogen N5.0) was 342.6 and 335.8  $\text{mg m}^{-3}$  in single component gas, and 317.8 and 341.9  $\text{mg m}^{-3}$  in binary gas mixture, respectively. The adsorption experiment was stopped when the effluent concentration matched the influent concentration for at least 10 min. The adsorption capacity ( $q$ ) of adsorbent bed was calculated by the following equation:

$$q = \frac{F \cdot C_0}{m} \int_0^t \left(1 - \frac{C_t}{C_0}\right) dt \quad (2)$$

where the  $F$  is the gas flowrate,  $m$  is the mass of the adsorbent,  $C_0$  and  $C_t$  are adsorbate concentrations at the inlet and outlet of the column, respectively. Breakthrough adsorption capacity ( $q_b$ ) was calculated for a  $t$  when  $C_t/C_0$  is equal to 0.1, and maximum adsorption capacity ( $q_f$ ) for  $t$  when  $C_t = C_0$ . For a binary component mixture adsorption, the abovementioned equation had to be modified to accommodate the roll-up effect:

$$q = \frac{F \cdot C_0}{m} \cdot \left( \int_0^t \left(1 - \frac{C_t}{C_0}\right) dt - \int_{t_1}^{t_f} \left(\frac{C_t}{C_0} - 1\right) dt \right) \quad (3)$$

where  $t_1$  and  $t_f$  are the start and end times of the roll-up effect. The height of the mass transfer zone ( $H_{MTZ}$ ) was calculated from Eq. (4):

$$H_{MTZ} = L \left( \frac{t_f - t_b}{t_e} \right) \quad (4)$$

where  $t_f$  and  $t_b$  are saturation and breakthrough time, respectively. The selectivity of benzene/cyclohexane separation was calculated from binary component breakthrough analysis with following equation:

$$\alpha_{Bz/Cy} = \frac{q_{b,Bz} \cdot y_{Cy}}{q_{b,Cy} \cdot y_{Bz}} \quad (5)$$

Recyclability was assessed by measuring breakthrough adsorption capacities for ten consecutive adsorption/desorption cycles. After each adsorption step, the adsorbent bed was regenerated (desorption step) at 250 °C under 5  $\text{mL min}^{-1}$  nitrogen flow to the moment when the detector signal reaches the baseline.

#### 2.9. DFT calculations

Reduced graphene oxide (RGO) was theoretically modelled, within dispersion-corrected density functional theory (DFT), by means of polycyclic aromatic hydrocarbon (PAH) models. In addition, benzene,

cyclohexane, and cyclohexene were modelled within the same level of theory as discussed below. All the structures analysed were optimized within the generalized gradient approximation (GGA) by the exchange correlation functional of Perdew, Burke and Ernzerhof (PBE) [48]. Also, a triple- $\zeta$  valence basis set with a set of polarization functions, named as def2-TZVP [49], was used to model the electrons in the molecular orbitals. Also, dispersion interactions were taken into account by the Grimme's correction term D3, with the damping function of Becke and Johnson (BJ) [50]. The full method, hereinafter named as PBE-D3(BJ)/def2-TZVP, was used as implemented in the quantum chemistry package Turbomole version 7.7 [51]. Spin-unrestricted calculations were performed in all cases. The highest occupied molecular orbital (HOMO) as well as the lowest unoccupied molecular orbital (LUMO) were plotted, on isosurfaces with 0.02 a.u. of electron density, by using the wavefunction of the correspondent system in the visualizer Avogadro version 1.2.0 [52]. Similarly, the electrostatic potential was mapped on the van der Waals surface, with 0.0004 a.u. of electron density.

### 3. Results and discussion

#### 3.1. Aerogels characterization

Aerogels samples were prepared by chemical reduction induced self-assembly of GO. LAA and BS are typical reductants used in the process. As for the DTN, to the best of our knowledge, it is the first report informing about its use for synthesis of rGOA. For LAA and BS, the reductant to GO ratio was set to 4:1 and 1:1, respectively. In case of DTN aided process, the ratio was set to 2:1 because textural analysis revealed that it yielded the most developed surface area of the aerogel. The plot of surface area against the DTN amount is presented in Figure S1. The density of the rGOAs was in the range of 20 mg cm<sup>-3</sup>. For rGOA\_DTN, rGOA\_BS and rGOA\_LAA, it was around 19.6, 19.9, and 20.1. The values are in agreement with data reported in the literature [53].

The reductant to GO ratio is reported on a mass basis in the literature. However, because the amount of oxygen groups on the GO surface was known from the Boehm titration, the abovementioned values were recalculated to express the reductant to GO ratio as moles of reductant to moles of oxygen-containing groups of GO. In this way, ratios for LAA, BS and DTN are 10.0, 4.2 and 5.1, respectively. Because carboxylic groups were the main constituents of the GO, their concentration was used to monitor the reduction extent. As a result of reduction, the carboxylic group concentration dropped from 2.193 mmol g<sup>-1</sup> to 0.882, 0.438 and 0.127 mmol g<sup>-1</sup> for rGOA\_LAA, rGOA\_BS and rGOA\_DTN respectively. The procedure of Boehm titration is provided in Text S2.

The microstructure of aerogels was observed by SEM. For instance, Fig. 3 shows that macropores with size of micrometers are closely stacked with walls consisted of partially overlapping, randomly oriented rGO flakes producing a significant amount of mesopores among these flakes. Generally, aerogels had multi-layered, interconnected 3D porous structure with hierarchical pores and wrinkled texture.

The texture of rGOA samples was analysed by the nitrogen (77 K) adsorption-desorption isotherm, which are presented in Fig. 4a. For all samples, the measured adsorption isotherms exhibited type II behavior, with H3 hysteresis loop. Such isotherm shape is typically given by materials constructed of aggregates of platy particles with slit shape pores and macropores present [54]. It agrees with the structure of rGOA reported in literature for aerogels synthesized with method similar to the one employed in this work. Such structure is created by interconnected, randomly stacked and entangled rGO flakes [55]. Values of BET surface area calculated from nitrogen adsorption isotherms are presented in Table 2. The lowest value of 261.15 m<sup>2</sup>/g was measured for aerogel sample synthesized with the aid of LAA and it was in good accordance with the one reported in the literature [30]. Interestingly, there was marginal difference between rGOA\_LAA sample and the GO in terms of surface area. Together with FTIR and Boehm titration results, it suggests that l-ascorbic acid plays only the role of reductant and facilitates the self-assembly of GO flakes but the porous structure is contoured by formation of ice crystals in the freeze-drying process. The situation looks different for other reductants. For instance, the introduction of BS and DTN affects not only chemical structure but porosity as well. The highest surface area of 457.75 m<sup>2</sup>/g was measured for the rGOA\_DTN while for the rGOA\_BS sample it was 390.43 m<sup>2</sup>/g.

A barely visible hysteresis loop in the isotherm of rGOA\_LAA indicates that the dimensions of its pores are in the range of macropores. Contrary to the LAA, other reductants used for rGOA synthesis play a role in the development of the porous structure. For both, rGOA\_BS and rGOA\_DTN distinct hysteresis loops can be observed, which are a result of mesopores presence. Moreover, a more noticeable knee at low  $p/p^0$  (<0.1) may reveal formation of micropores [43] but the t-plot method did not confirm the presence of micropores. If some micropores are present, their volume is insignificant compared to meso and macropores, therefore, both aerogels can be considered as meso-macroporous materials. Isotherms analysis revealed that the highest mesopores surface area was obtained for the rGOA\_DTN (152.2 m<sup>2</sup>/g) followed by rGOA\_LAA and rGOA\_BS (144.4 and 134.0 m<sup>2</sup>/g, respectively).

Concerning rGOAs, it is common to supply results of nitrogen adsorption analysis with pores size distribution (PSD) and total pore volume. However, lack of limiting adsorption at high  $p/p^0$  in type II isotherms with H3 loops make difficult a reliable assessment of both mentioned parameters [54,56]. Additionally, a special caution must be taken when reviewing literature because in some works the nitrogen isotherms of aerogels samples are falsely described as type IV [33,37] or V [41], while this types are characterized by the clear plateau at  $p/p^0 = 1$ . For this reason, we don't provide the total pore volume in this work and PSD for mesopore range is provided in the SI only for comparison purposes between samples (Figure S2). The use of l-ascorbic acid as reductant resulted in rather uniform distribution of mesopores ranged from 2 to 50 nm with the small maximum located around the pore size of 23 nm. Sodium dithionite and sodium bisulfite created a rather different (narrower) pore size distribution with most of the nitrogen adsorption

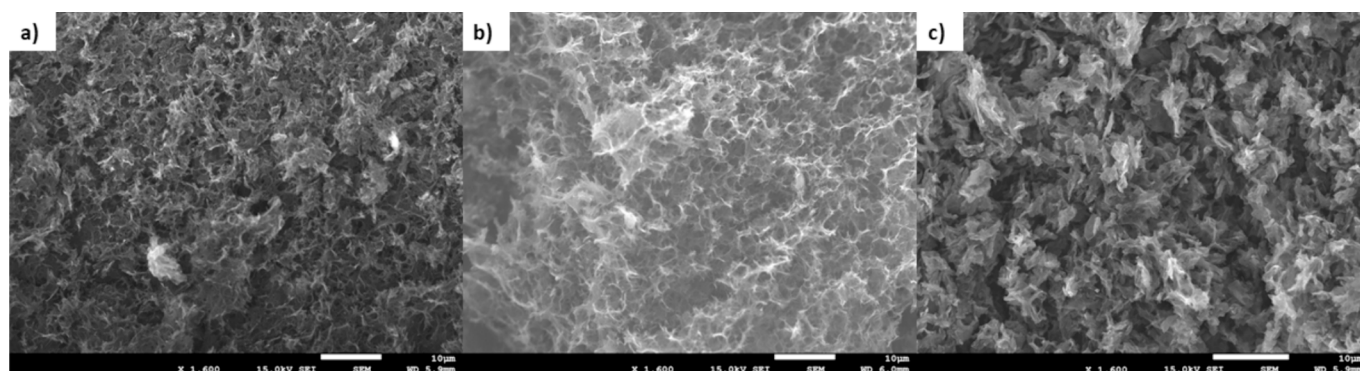


Fig. 3. SEM images of a) rGOA\_LAA, b) rGOA\_BS, c) rGOA\_DTN.

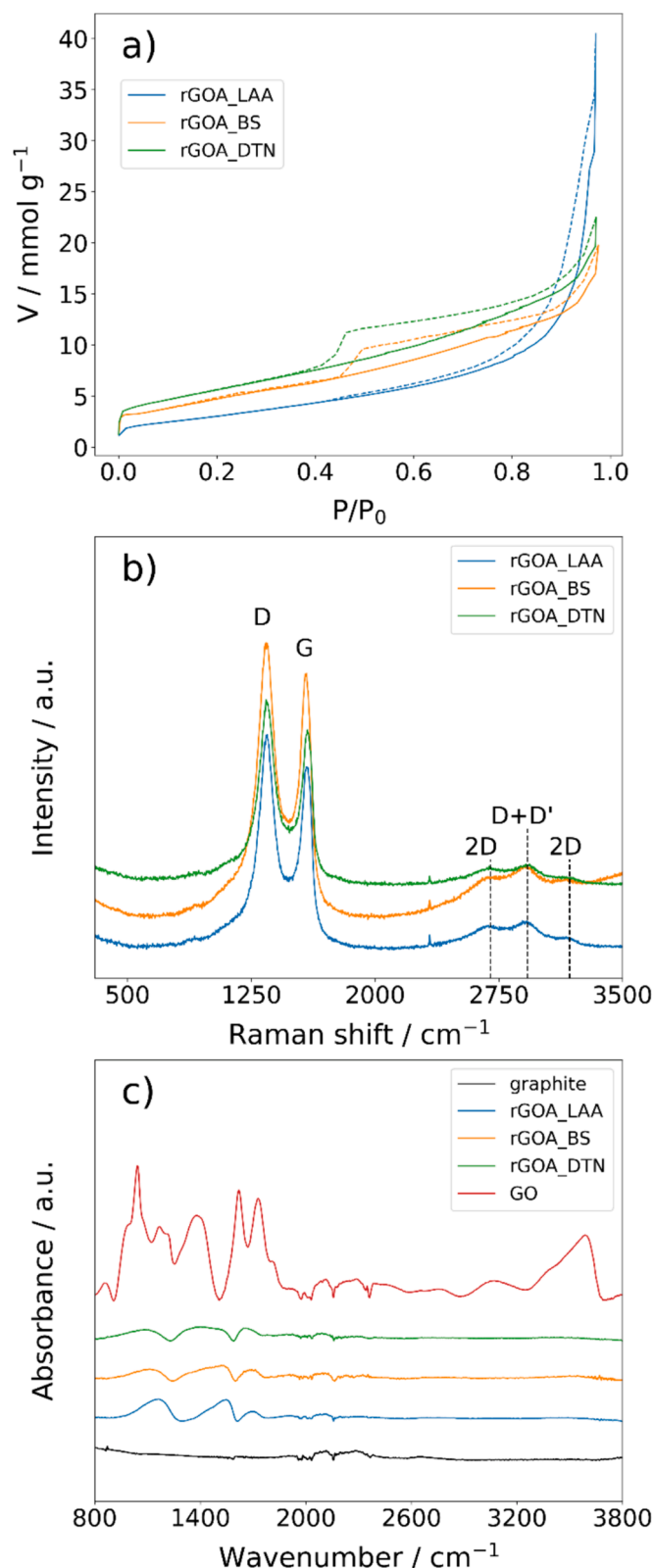


Fig. 4. Results of physicochemical characterization of adsorbents: a) nitrogen adsorption isotherms at 77 K (dashed line represents desorption branch), b) Raman spectra, c) FTIR spectra of reduced graphene oxide aerogels.

occurring in the pores smaller than 10 nm. The rGOA\_BS and rGOA\_DTN have peaks at around 3.96 nm and 3.72 nm, respectively. Considering results of the textural analysis, the rGOA\_DTN sample is the most promising for adsorptive separation of benzene and cyclohexane.

The self-assembly process of GO flakes is driven by reduction of oxygen-containing functional groups and formation of non-covalent interactions. This fact can be confirmed by Raman and FTIR spectra presented in Fig. 4b and Fig. 4c. Raman spectra are typical for rGOA samples and are dominated by the D and G bands at around  $1340\text{ cm}^{-1}$  and  $1584\text{ cm}^{-1}$ . The presence of D band is attributed to the  $\text{sp}^3$  carbon and defects in the GO structure while G band to partially disordered  $\text{sp}^2$  carbon domains. The position of the D band was the same for all rGOA samples while for G band a gradual shift to higher wavenumbers was observed in the following order: rGOA\_BS ( $1579\text{ cm}^{-1}$ ) < rGOA\_LAA ( $1584\text{ cm}^{-1}$ ) < rGOA\_DTN ( $1592\text{ cm}^{-1}$ ). This direction of the shift can be caused by the higher proportion of isolated double bonds, conversely the down shift of G band indicates restoration of hexagonal, graphitic order. The intensity ratio of D and G band increased after reduction and formation of aerogels, compared to GO. Increase of  $I_D/I_G$  value indicates restoration of  $\pi$ - $\pi$  conjugated structure with defects by formation of  $\text{sp}^2$  domains that are smaller compared to GO but more in number. The highest value was measured for rGOA\_DTN (1.21), while the lowest reduction was achieved for rGOA\_BS (1.12) – the data is provided in Table 2. In the FTIR spectra some minimal contribution from the oxygen containing functionalities can be observed but overall, the rGOAs spectra are more similar to graphite rather than to GO spectrum. The abundant oxygen-containing groups in GO structure gave a strong absorption bands in the  $3000\text{--}3700\text{ cm}^{-1}$  (hydroxyl groups, either from phenol or carboxylic configuration),  $1500\text{--}2000\text{ cm}^{-1}$  (overlapping of carboxyl and ketones vibrational modes, as well as C = C carbons within graphitic domains), and  $800\text{--}1500\text{ cm}^{-1}$  (fingerprint region generated by different oxygen functionalities, e.g., epoxides, ether or lactols) regions. For rGOAs, only small absorption bands are observed in the fingerprint part of the spectra, while in the range above  $3000\text{ cm}^{-1}$ , no absorption of IR radiation by  $-\text{OH}$  groups is observed. It indicates efficient reduction of oxygen-containing functional groups in the process of aerogels self-assembly.

Structural transformation of aerogels surface should have an impact on the capability for intermolecular interactions and can be measured by IGC, e.g., by the dispersive component of the surface free energy ( $\gamma_s^D$ ). It can be used as a measure of how active material surface is and is typically determined for near-zero surface coverage. Fig. 5 shows a distribution of  $\gamma_s^D$  over the surface coverage ( $\theta$ ) in the range of 0.005–0.1. Initially, the  $\gamma_s^D$  value is decreasing in the following order rGOA\_DTN > rGOA\_BS > rGOA\_LAA. Considerable values at low  $\theta$  are caused by preferential adsorption of probe molecules on highest energy sites. Additionally, if these adsorption sites are located in mesopores, a cooperative effect of adjacent walls may be observed. As the part of the surface occupied by the adsorbate is increasing, the  $\gamma_s^D$  values are lowering and a shift in the order of the aerogels with the highest values of dispersive component was observed. The rGOA\_LAA demonstrated the uppermost  $\gamma_s^D$  of  $151 \pm 2\text{ mJ m}^{-2}$  followed by rGOA\_BS ( $107 \pm 1$ ) and rGOA\_DTN ( $80 \pm 1$ ). The steepest decline was observed for rGOA\_DTN and rGOA\_BS samples, while for rGOA\_LAA, the change was gradual indicating that the surface of the sample reduced with *l*-ascorbic acid is the most homogenous.

Dispersive interactions would be a main contributor to the total intermolecular interaction in case of pristine graphene. The theoretical modelling within dispersion-corrected DFT revealed that the lack of polar groups leads to neutral electrostatic potential at the centre of each carbon ring, but with negative regions around the carbon atoms. In contrast, hydrogen atoms at the edges are obtained as the regions with positive electrostatic potential are the most prone to interactions. The electrostatic potential (ESP) maps of pristine and oxygen group containing rGO models are presented in Fig. 6a. If modified with oxygen functionalities (e.g., epoxy or hydroxyl), a significant change in the

**Table 2**  
Properties of rGOA adsorbents.

Sample	BET area / m <sup>2</sup> g <sup>-1</sup>	COOH / mmol g <sup>-1</sup>	I <sub>D</sub> /I <sub>G</sub>	γ <sub>S</sub> <sup>D</sup> / mJ m <sup>-2</sup>	I <sub>M,cycloC8</sub>	I <sub>M,isoC8</sub>	-ΔH <sub>A,Bz</sub> / kJ mol <sup>-1</sup>	-ΔH <sub>A,Cy</sub> / kJ mol <sup>-1</sup>
GO	282.6	2.193 ± 0.025	0.79	–	–	–	–	–
rGOA_LAA	262.7	0.882 ± 0.005	1.16	231 ± 2	0.043	0.058	46.1 ± 7.3	–
rGOA_BS	395.7	0.438 ± 0.043	1.12	240 ± 2	0.065	0.101	35.1 ± 5.0	53.7 ± 4.3
rGOA_DTN	461.2	0.127 ± 0.014	1.21	251 ± 1	0.085	0.123	52.9 ± 7.6	65.7 ± 3.1

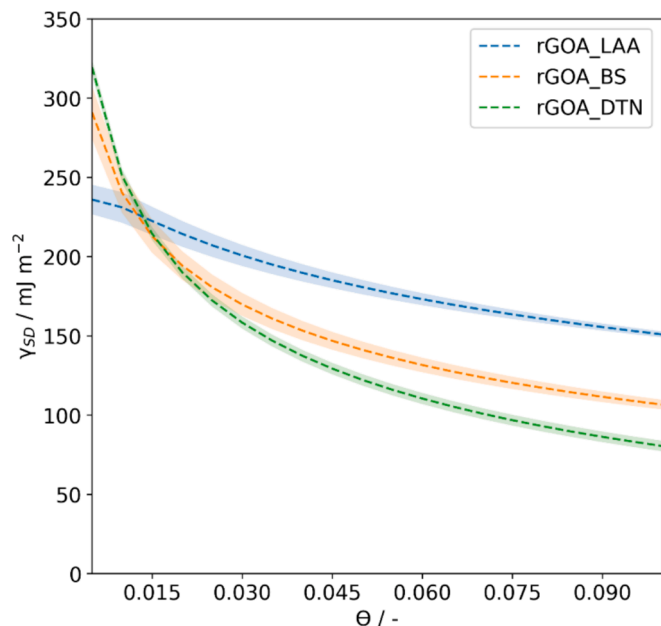


**Fig. 5.** Dispersive component (with 95% confidence interval as shaded area) of the surface free energy distribution for rGOAs samples.

charge distribution is observed. For example, epoxy group creates an accumulation of negative charge around oneself, but the charge distribution at edges remains almost unaltered, compared to pristine graphene (Fig. 6b). For -OH group, a major accumulation of charge took place near the functional group, creating a large zone with negative electrostatic potential between -OH and the closest corner of the graphene model, and the lone pairs on the hydroxyl group are susceptible for molecular interaction. In contrast, the hydrogen atom of the -OH group is obtained as the region with highest electrostatic potential (Fig. 6c). In case of a rGO model having both types of oxygen functionalities (Fig. 6d), an extended accumulation of charge is observed from the corners to the functional groups. Moreover, the HOMO-LUMO gap was reduced up to 0.371 eV, in comparison with the 0.644, 0.622 and 0.405 eV calculated for pristine, epoxy, and hydroxyl containing models, respectively. Such reduction of energy gap indicates existence of stronger intermolecular interactions for the rGO with specific, oxygen-containing functional groups [57].

In view of the foregoing, the rGOA should be able to attract adsorbate molecules through electron donor and electron acceptor interactions,

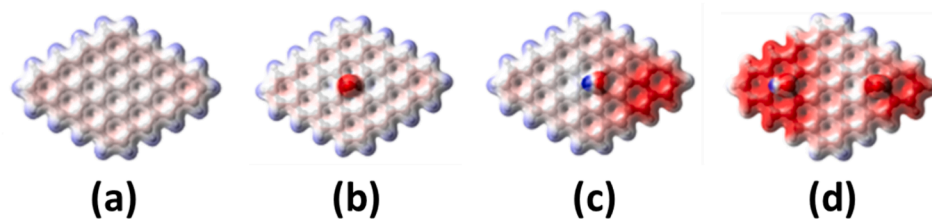


**Fig. 6.** Electrostatic potential maps for a) pristine graphene, b) modified with epoxy group, c) modified with hydroxyl group and d) rGO. Red colour denotes regions with negative potential, whereas positive ones are blue coloured. ESP mapped on isosurfaces with 0.02 a.u. of electron density.

depending on the nature of adsorbate. Fig. 7 shows the ESP maps of benzene and cyclohexane molecule. For benzene, the accumulation of charge is observed near the carbon ring, while hydrogen atoms are regions with the highest electrostatic potential. Similar distribution is observed for cyclohexane where the accumulation of charge takes place around the C-C bonds, whereas hydrogen atoms exhibit the highest ESP values. However, the energy gap of benzene (5.132 eV) is about 2 eV lower than that of cyclohexane (7.366 and 7.176 for chair and boat conformations, respectively). Thus, the ring of benzene molecules should be more prone to π···C-H interaction with a positive charge of the hydrogen atoms located at the edges of rGO [58]. Conversely, the positively charged hydrogens of benzene can form complexes with rGO carbon lattice such as edge-to-face (T-shaped) or with negative charge accumulated close to oxygen-containing functional groups. Cyclohexane can be capable of similar interaction but with lower magnitude.

The benzene and cyclohexane interactions were examined with IGC by measuring the retention of single components on aerogels samples. Fig. 8 presents plots of free energies of adsorption (ΔG<sub>A</sub>) of benzene and cyclohexane as a function of the topological index (X<sub>T</sub>) as the molecular descriptor – it takes into account the geometry, as well as local electron density of the probe. The contribution of specific interactions can be deduced based on the position of benzene and cyclohexane points in reference to n-alkane line. If present, these points should be located above alkane line and the magnitude of specific interaction can be calculated as the distance between the probe point and reference line. For all samples, benzene points are located above respective n-alkane lines indicating presence of specific interactions. The strongest contribution to overall ΔG<sub>A</sub> was measured for LAA (10.90 kJ mol<sup>-1</sup>). For rGOA\_DTN and rGOA\_BS, benzene specific interactions had almost the same strength (7.70 and 7.71 kJ mol<sup>-1</sup>, respectively). The opposite is observed for cyclohexane. For all samples, its ΔG<sub>A</sub> is less than what would be expected for hypothetical n-alkane with the same X<sub>T</sub>. It suggests that cyclohexane molecules access to the rGOAs surface is partially restricted due to size exclusion effects.

One type of barrier is created by pores of different dimensions that will limit the diffusion of bulkier molecules – cyclohexane in the case of benzene and cyclohexane separation. The second source of the size exclusion effects can be structural defects of the surface at the molecular level. The magnitude of this effect can be described by nanomorphological index (I<sub>M</sub>), which is a measure of what part of the solid surface can be accessed by the bulky probe (branched alkane), compared to its linear analogue – a value of 1 indicates a molecularly flat surface equally accessible to both branched and linear alkanes. I<sub>M</sub> values measured with isooctane (I<sub>M,isoC8</sub>) and cyclooctane (I<sub>M,cycloC8</sub>) are presented in Table 2. For all aerogels, I<sub>M</sub> values lower than 0.125 were

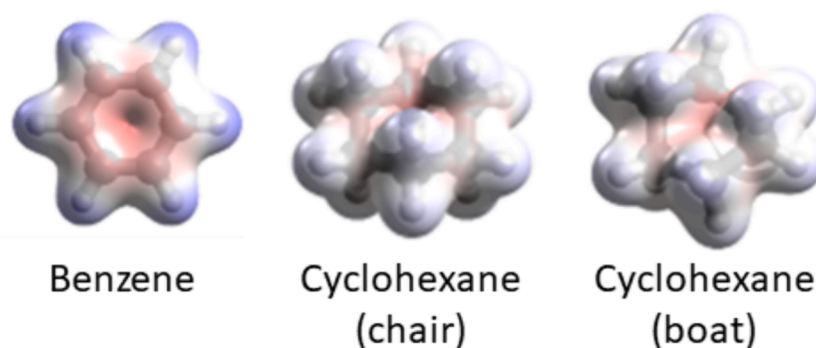


**Fig. 7.** Electrostatic potential (ESP) maps for benzene and cyclohexane (boat and chair conformations) molecules. Red colour denotes regions with negative potential, whereas positive ones are blue coloured. ESP mapped on isosurfaces with 0.02 a.u. of electron density.

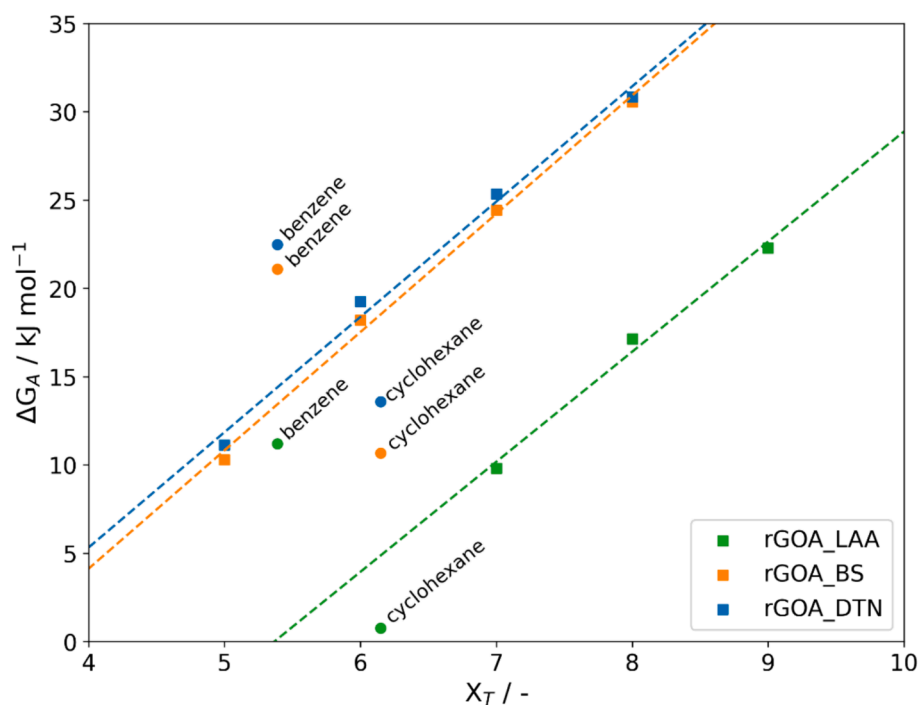


**Fig. 8.** Variation of  $\Delta G_A$  of n-alkanes, cyclohexane and benzene probes as a function of topological index ( $X_T$ ) for rGOAs at 453 K and  $\theta = 0.01$ .

observed regardless of the probe used for measurement, indicating pronounced steric constraints and exclusion effects for branched, bulky molecules. The least accessible surface (the lowest  $I_M$ ) was exhibited by rGOA\_LAA samples, followed by rGOA\_BS and rGOA\_DTN. Such low values of  $I_M$  can also justify high surface energy of aerogels, which comes not only from cooperative effect of adjacent walls in pores as mentioned before, but also from multiple interactions of alkanes molecules with nano-rough surface. Similar observation about formation of nanoscale roughness in partially reduced rGOAs have been reported in the literature [59].

From the  $\Delta G_A$  values measured at different temperatures, the enthalpy of adsorption of cyclohexane ( $\Delta H_{A,Cy}$ ) and benzene ( $\Delta H_{A,Bz}$ ) was calculated. The values are given in Table 2. For both, benzene and cyclohexane, absolute values of enthalpy of adsorption were higher than their enthalpies of vaporization (22.68 and 23.59 kJ mol<sup>-1</sup>, respectively). According to measured enthalpies of adsorption, rGOA\_DTN had the highest affinity to benzene ( $-52.9 \pm 7.6$  kJ mol<sup>-1</sup>), followed by rGOA\_LAA ( $-46.1 \pm 7.3$  kJ mol<sup>-1</sup>) and rGOA\_NaHSO<sub>3</sub> ( $-35.1 \pm 5.0$  kJ mol<sup>-1</sup>). All mentioned values pointed to physisorption as a mechanism of adsorption. Comparison with results of Raman spectroscopy revealed the positive correlation with  $I_D/I_G$  ratio ( $R^2 = 0.961$ ). With the increased

number of  $sp^2$  domains (the higher  $I_D/I_G$  ratio), the enthalpy of benzene adsorption increases. It agrees with previously discussed results of DFT calculations. For cyclohexane, only data for rGOA\_NaHSO<sub>3</sub> and rGOA\_DTN is available (the retention on rGOA\_LAA at experimental conditions was insufficient). The  $-\Delta H_{A,Cy}$  was slightly higher compared to  $-\Delta H_{A,Bz}$ . It may be caused by the fact that if adsorption of cyclohexane is to happen, it can only take place on the most energetic sites. Moreover, it cannot be ruled out that flat molecule of benzene is also excluded from the nanorough surface of rGOA but the effect is compensated by specific interactions. In contrast to benzene, the cyclohexane molecule has the ability to undergo configuration changes to maximize its C-H... $\pi$  interactions [14].

Apart from  $-\Delta H_A$  values, the affinity of cyclohexane and benzene molecules to rGOAs were estimated based on TPD. In contrast to IGC measurements, the energy of desorption ( $E_d$ ) determined with TPD is a representation of a binding energy of a larger fraction of adsorption sites. Peak temperatures of TPD curves and desorption activation energies of benzene and cyclohexane are listed in Table 3. The affinity of rGOAs surface for cyclohexane is similar regardless of the reductant used in the synthesis as the  $E_d$  values are almost the same. However, for benzene, there is a significant difference between different aerogel



**Table 3**

Desorption peak temperatures ( $T_p$ , K) of TPD curves at different heating rates and calculated desorption activation energies of benzene and cyclohexane on the rGOAs.

Sample	$\beta_H / \text{K min}^{-1}$			$E_d / \text{kJ/mol}$
	2	5	8	
<b>Benzene</b>				
rGOA_LAA	419.2	440.5	451.2	$60.6 \pm 1.5$
rGOA_BS	415.7	445.8	455.7	$45.4 \pm 6.1$
rGOA_DTN	378.1	433.2	450.0	$19.2 \pm 3.7$
<b>Cyclohexane</b>				
rGOA_LAA	438.4	461.5	481.1	$49.7 \pm 6.4$
rGOA_BS	404.5	430.9	444.4	$44.7 \pm 1.2$
rGOA_DTN	412.0	434.4	450.8	$48.5 \pm 4.1$

samples. The highest  $E_d$  was measured for rGOA\_LAA ( $60.6 \pm 1.5 \text{ kJ mol}^{-1}$ ) while the lowest for rGOA\_DTN ( $19.2 \pm 3.7 \text{ kJ mol}^{-1}$ ), and for rGOA\_BS, the value in between previous samples was observed ( $45.4 \pm 6.1 \text{ kJ mol}^{-1}$ ). The TPD curves for all rGOAs are presented in Figure S3.

The highest binding affinity difference between benzene and cyclohexane was observed for rGOA\_LAA. Based on TPD results, the ratio of their  $E_d$  was  $1.22 \pm 0.19$ , while for rGOA\_NaHSO<sub>3</sub> and rGOA\_DTN, it was  $1.02 \pm 0.16$  and  $0.40 \pm 0.11$ , respectively. Judging the rGOAs ability to selectively separate benzene from cyclohexane solely by these values should result in the selection of rGOA\_LAA as the most suitable adsorbent. However, the textural properties cannot be neglected. The adsorbed amount is largely a function of specific surface and the one of rGOA\_DTN is by 75 % higher compared to rGOA\_LAA. Adding to this the limited accessibility of cyclohexane molecules to the surface, caused by the nanoroughness, the rGOA\_DTN might prove to be a superior adsorbent.

This reasoning is supported by the desorption isotherm measured with IGC-FC at 453 K. The rGOA\_DTN adsorption capacity ( $q_s$ ) of benzene, deduced from modelling the experimental data with the Sips isotherm model, was  $177.83 \mu\text{mol g}^{-1}$  compared to  $109.33$  and  $14.46 \mu\text{mol g}^{-1}$  for rGOA\_NaHSO<sub>3</sub> and rGOA\_LAA, respectively – the adsorption capacity of rGOA\_DTN was over 12 times higher than that of rGOA\_LAA. The cyclohexane  $q_s$  was very similar for both rGOA\_DTN and rGOA\_NaHSO<sub>3</sub> ( $21.71$  and  $29.52 \mu\text{mol g}^{-1}$ , respectively), while for rGOA\_LAA, the cyclohexane adsorption was insufficient to obtain reliable data. The results of Sips isotherm model fitting to experimental data are presented in Table 4. The desorption isotherms can be found in Figure S4.

### 3.2. Single component dynamic adsorption

Adsorption performance measured in dynamic conditions is crucial for evaluation of the adsorbent applicability because experimental conditions can play a significant role in separation. For example, in the case of separating hexane isomers on ZIF-8 (zeolitic imidazolate

**Table 4**

Sips isotherm parameters for the adsorption of benzene and cyclohexane on rGOAs at 453 K.

	rGOA_LAA	rGOA_NaHSO <sub>3</sub>	rGOA_DTN
<b>Benzene</b>			
$q_s / \mu\text{mol g}^{-1}$	$14.46 \pm 0.60$	$109.33 \pm 2.78$	$177.83 \pm 7.77$
$K_s / \text{Pa}^{-1} \cdot 10^3$	$45.65 \pm 4.51$	$28.91 \pm 1.63$	$21.95 \pm 1.74$
$R^2$	0.981	0.985	0.991
<b>Cyclohexane</b>			
$q_s / \mu\text{mol g}^{-1}$	–	$29.52 \pm 1.16$	$21.71 \pm 1.13$
$K_s / \text{Pa}^{-1}$	–	$32.78 \pm 2.26$	$58.48 \pm 3.98$
$R^2$	–	0.994	0.999

framework-based adsorbent), it was found out that while a high selectivity of n-hexane over branched isomers was observed during the breakthrough experiment, branched isomers exhibited a higher extent of adsorption than n-hexane in static adsorption. However, the diffusional parameters calculated from static adsorption data still pointed out to considerable selectivity between hexane isomers [60]. Thus, experimental conditions can determine which factor, *i.e.*, kinetic or thermodynamic will play a major role in separation of adsorbates.

To evaluate the applicability of adsorbents in cyclic adsorption-separation processes, fixed-bed breakthrough curves were measured for cyclohexane and benzene as single components in nitrogen at a range of temperatures (50–90 °C). Nitrogen was assumed to be noninteracting component at the experimental conditions. Results of breakthrough experiments are presented in Fig. 9 and Table 5.

The selectivity of all rGOA samples toward benzene is evident from breakthrough curves. Aerogel reduced with *l*-ascorbic acid (rGOA\_LAA) had the uppermost difference between benzene and cyclohexane breakthrough adsorption capacity ( $q_b$ ) of  $6.38 \pm 0.09$ . For rGOA\_NaHSO<sub>3</sub> and rGOA\_DTN, this value decreased to  $2.01 \pm 0.08$  and  $2.07 \pm 0.03$ , respectively. However, in terms of absolute adsorption capacity, samples reduced with BS and DTN exceed rGOA\_LAA significantly. The rGOA\_BS and rGOA\_DTN had over 5 and 6 times higher  $q_b$  for benzene respectively, while for cyclohexane, it was over 16 and 20 times higher. The total adsorption capacity ( $q_t$ ) of benzene and cyclohexane followed a similar trend and was the highest for rGOA\_DTN and the lowest for rGOA\_LAA. Moreover, both rGOA\_NaHSO<sub>3</sub> and rGOA\_DTN had much shorter mass transfer zone ( $H_{MTZ}$ ), compared to rGOA\_LAA. The lowest value of  $H_{MTZ}$  (0.73 cm for cyclohexane and 1.11 cm for benzene) was observed for rGOA\_DTN, so it can be expected that this material will ensure the most efficient utilization of the adsorbent bed capacity.

The breakthrough data was fitted with the Yoon-Nelson model to describe the dynamic behaviour of adsorption columns with rGOA samples. This model is typically used in the literature to address the breakthrough of vapours of organic adsorbates on different adsorbents, but especially on carbonaceous adsorbents. The values of  $k_{YN}$  and  $\tau$ , together with correlation coefficients, calculated for breakthrough curves measured at 50 °C are given in Table 6. Data for all breakthrough curves determined at different temperatures is provided in Table S1. Coefficient of determination values are found to be above 0.99 indicating appropriate fit of the model. The adsorption rate constant for benzene, as well as for cyclohexane, increased in the following order: rGOA\_BS < rGOA\_DTN < rGOA\_LAA. The highest value of  $k_{YN}$  was observed for rGOA\_LAA sample. For cyclohexane and benzene, it was over 3 and almost 2 times higher, compared to other rGOA tested. This fact may be attributed to the macroporous structure or rGOA\_LAA leading to lower pore diffusion resistance.

Considering the above, the rGOA\_DTN was selected for binary adsorption test. The lower ratio of benzene and cyclohexane breakthrough adsorption capacities has been selected as a trade-off for longer service time of adsorption column filled with rGOA\_DTN adsorbent.

Comparison of the breakthrough adsorption capacity with results of the textural analysis revealed that the adsorption capacity of aerogels, for both benzene and cyclohexane, correlates good with the surface area ( $R^2 = 0.986$  and  $0.996$  for cyclohexane and benzene respectively). Moreover, when the surface area was divided into mesopores and macropores, the excellent correlation with the macropores surface area was observed ( $R^2 = 0.999$  for both adsorbates) but not with the mesopores surface area ( $R^2 < 0.05$  for both adsorbates). Knowing that the diameter of benzene and cyclohexane molecules is less than 1 nm and rGOAs pores are above 2 nm, the pore size of adsorbents is not responsible for the significant difference between cyclohexane and benzene adsorption. While the extent of adsorption of adsorbate will increase with the surface area because more adsorption centres will be available, the reason for selectivity of adsorption are thermodynamic factors (interactions with the aerogels surface) and surface roughness on a molecular level.

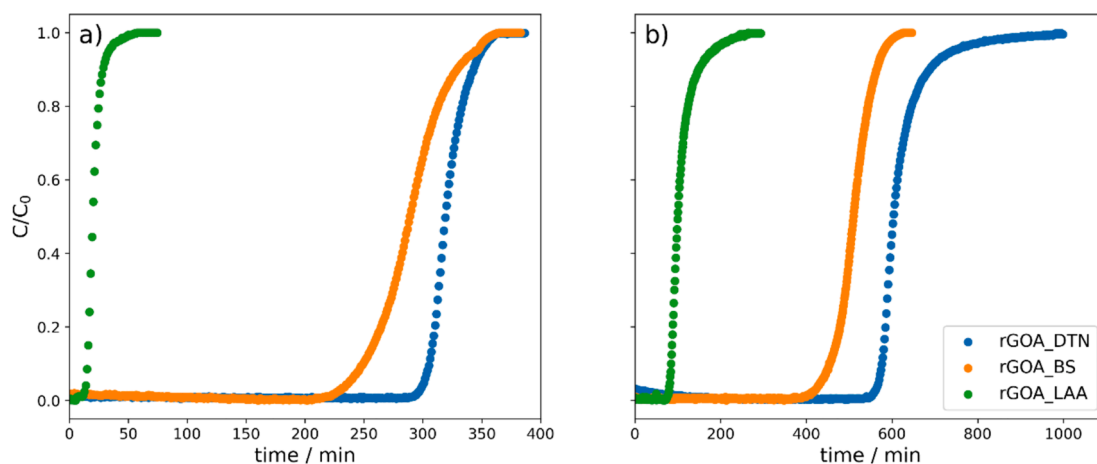


Fig. 9. Single component breakthrough curves for a) cyclohexane and b) benzene measured at 50 °C on rGOA samples.

Table 5

Results of single component breakthrough curves of the adsorption at 50 °C of cyclohexane and benzene using rGOA adsorbents.

Sample	Cyclohexane			Benzene		
	$q_b / \mu\text{mol/g}$	$q_t / \mu\text{mol/g}$	$H_{MTZ} / \text{cm}$	$q_b / \mu\text{mol/g}$	$q_t / \mu\text{mol/g}$	$H_{MTZ} / \text{cm}$
rGOA_LAA	9.3 ± 0.1	13.3 ± 0.2	2.94 ± 0.12	59.3 ± 0.2	78.2 ± 0.3	2.92 ± 0.15
rGOA_BS	151.0 ± 2.7	176.4 ± 3.3	1.38 ± 0.02	302.8 ± 6.4	345.3 ± 3.1	1.13 ± 0.06
rGOA_DTN	191.4 ± 1.9	202.6 ± 2.6	0.73 ± 0.09	395.7 ± 2.2	425.1 ± 2.5	1.11 ± 0.02

Table 6

Parameters of Yoon-Nelson model fitted to single component breakthrough data collected at 50 °C.

	$k_{YN} / \text{min}^{-1}$	$\tau / \text{min}$	$R^2$
<b>cyclohexane</b>			
rGOA_LAA	0.329 ± 0.012	20.4 ± 0.1	0.996
rGOA_BS	0.058 ± 0.001	286.0 ± 2.9	0.999
rGOA_DTN	0.097 ± 0.012	326.6 ± 3.1	0.997
<b>benzene</b>			
rGOA_LAA	0.070 ± 0.004	104.9 ± 1.6	0.991
rGOA_BS	0.039 ± 0.003	507.9 ± 2.4	0.999
rGOA_DTN	0.042 ± 0.001	613.0 ± 3.0	0.997

### 3.3. Binary component dynamic adsorption

Although essential for development of adsorbents, the single component data rarely give full clarity about the performance in the real-life applications. In multicomponent systems molecules compete for the same adsorption centres on a surface of an adsorbent. Therefore, data about competitive adsorption is crucial. Results of the binary-component breakthrough curve measurements are given in Fig. 10 and Table 7.

Fig. 10a shows breakthrough curves for benzene and cyclohexane. It can be divided into four zones. The following time values are accompanied by breakthrough volumes. First, up to ca. 200 min (56.8 L g<sup>-1</sup>) the rGOA\_DTN completely adsorbed both adsorbates and then the second zone – breakthrough – is observed for cyclohexane. While the adsorbent was no longer able to adsorb cyclohexane completely, the benzene was still entirely retained in the column until ca. 450 min (127.8 L g<sup>-1</sup>). Compared to single component adsorption, the  $q_b$  decreased from 191.4 and 395.7 to 126.6 and 306.3  $\mu\text{mol g}^{-1}$  (i.e. by 34

and 23 %), for cyclohexane and benzene respectively. Within the breakthrough zone, a third characteristic part can be distinguished, i.e. displacement zone which showed on the cyclohexane curve as a roll-up. It is a result of the competitive adsorption that is occurring over the course of the multicomponent adsorption process in the fixed-bed adsorbent. At that point, the cyclohexane concentration at the outlet exceeded the inlet concentration ( $C/C_0 > 1$ ) due to displacement of cyclohexane by benzene molecules with higher adsorption affinity. The amount of displaced cyclohexane ( $q_d$ ) was close 37  $\mu\text{mol g}^{-1}$ . Finally, the saturation zone is reached at around 550th min (156.3 L g<sup>-1</sup>) of analysis and the saturation capacity ( $q_d$ ) was 103.4 and 337.9  $\mu\text{mol g}^{-1}$  for cyclohexane and benzene, respectively. After that, the rGOA\_DTN required reactivation. In this work, the adsorption column was regenerated by thermal desorption. Fig. 10b presents results of reusability assessment based on  $q_b$  values measured for ten consecutive adsorption/desorption cycles. The stability of rGOA\_DTN performance was excellent as the breakthrough adsorption capacity and selectivity varied minimally. It is in line with prior experiences in IGC or single component breakthrough tests where no issues with reproducibility of results were encountered. Concluding, the rGOA\_DTN adsorbent exhibit high cyclic stability and should be able to provide long service life in adsorption processes.

### 3.4. Comparison with literature data and future outlook

The results of binary component breakthrough analysis are compared with literature data in Table 8. Because there is no standard procedure for breakthrough experiments, experimental conditions are specified in the table (adsorption temperature, gas flowrate and concentration of adsorbates). The rGOA\_DTN separation selectivity was at a similar level to mesoporous silica molecular sieve (KIT-6) and it surpasses ordered mesoporous silicas (MCM-41 and MCM-48), amorphous mesoporous silica (SBA-15), as well as covalent triazine framework adsorbent (CCTF-3). When compared to amorphous mesoporous silica calcined at 800 °C, the selectivity of rGOA\_DTN was lower, but the adsorption capacity was much higher for both benzene and cyclohexane. Among the adsorbents presented in Table 8, the activated carbon (E4 AC) had the uppermost selectivity of 2.52, as well as adsorption capacity. However, the selectivity of E4 AC sample was calculated simply as a ratio of total amounts of benzene and cyclohexane adsorbed. In this work, Eq. 4 was used which considers the molar fraction of adsorbate in the inlet gas, as well as breakthrough capacities of adsorbates which are more relevant for practical applications. If calculated similarly to E4 AC sample, the selectivity of rGOA\_DTN would be 3.40 instead of 2.09. Although rGOAs gained a lot of attention, the research on adsorption is very limited. To the best of our knowledge, no other reports about the

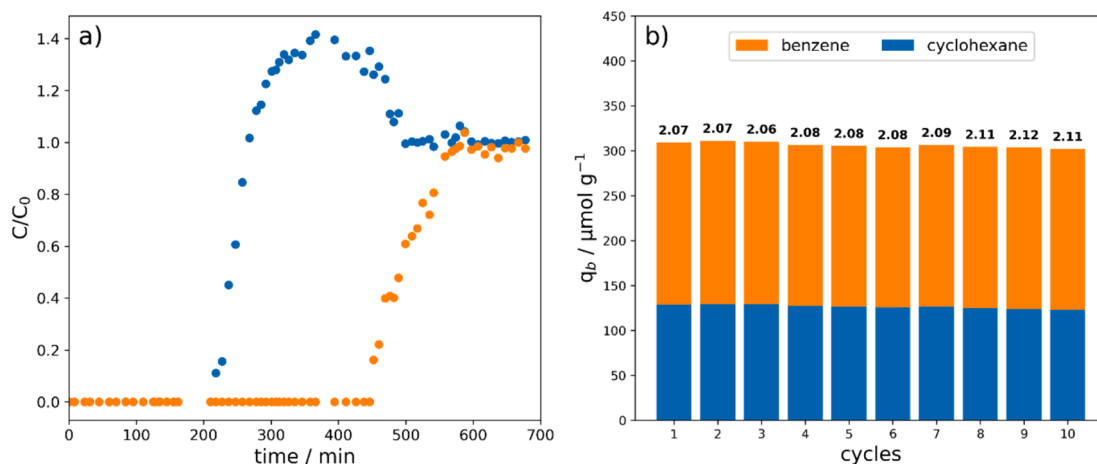


Fig. 10. A) binary component breakthrough curves and b) breakthrough adsorption capacities for ten consecutive adsorption/desorption cycles for rGOA\_DTN. Numbers above bars represent the benzene/cyclohexane selectivity.

Table 7

Results of analysis of binary component breakthrough curves for rGOA\_DTN at 50 °C.

Sample	Cyclohexane (Cy)				Benzene (Bz)			α <sub>Bz/Cy</sub>
	q <sub>b</sub> / μmol/g	q <sub>d</sub> / μmol/g	q <sub>t</sub> / μmol/g	H <sub>MRTz</sub> / cm	q <sub>b</sub> / μmol/g	q <sub>t</sub> / μmol/g	H <sub>MRTz</sub> / cm	
rGOA_DTN	126.6 ± 2.1	36.8 ± 1.2	103.4 ± 2.2	0.89 ± 0.02	306.3 ± 2.8	337.9 ± 2.7	0.99 ± 0.02	2.09 ± 0.02

Table 8

Comparison of adsorbents reported in the literature for the separation of benzene and cyclohexane.

Adsorbent	S <sub>BET</sub> / m <sup>2</sup> /g	Experimental conditions	Binary mixture adsorption capacity / mmol/g		α <sub>Bz/Cy</sub>	Ref
			Cyclohexane (Cy)	Benzene (Bz)		
E4 AC	894.05	50 °C, 5.5 mL min <sup>-1</sup> , 96 %*	12.83	32.36	2.52	[12]
SBA-2 (800 °C)	139.83	50 °C, 5 mL min <sup>-1</sup> , 96 %*	0.02	0.05	2.23	[10]
SBA-15	698	35 °C, 100 mL min <sup>-1</sup> , 500 ppm	0.32	0.54	1.69	[61]
MCM-41	1088		0.36	0.57	1.58	
MCM-48	1210		0.37	0.58	1.57	
KIT-6	912		0.32	0.67	2.09	
CCTF-3	207	25 °C, 54.688 mL min <sup>-1</sup> , 20000 ppm	0.31	0.60	1.90	[62]
rGOA_DTN	461.2	50 °C, 5 mL min <sup>-1</sup> , Benzene: 317.8 ppm, Cyclohexane: 341.9 ppm	0.10	0.34	3.40	This work

AC – activated carbon, SBA – amorphous mesoporous silica, MCM – ordered mesoporous silica, KIT – mesoporous silica molecular sieve, CCTF – covalent triazine framework,

\* - values back-calculated from reported data.

adsorptive separation of cyclohexane and benzene with the use of rGOAs are available.

The data presented in this work point out the capacity of rGOA to act as effective adsorbent in challenging separation scenarios. Moreover, there is much room for improvement in terms of aerogels selectivity and adsorption performance. The protocol of rGOA samples synthesis employed in this work was rather basic, without targeting for specific physicochemical properties desirable from the point of view of examined separation. The further development of rGOA adsorbents can progress in three main ways: texture (porosity) customization or physicochemical properties modification either on the synthesis stage or post-synthesis. The texture of aerogels can be tailored by directional freezing or differentiating solvent used for the process, e.g., replacing water to water/ethanol mixtures [63]. The chemical structure can be altered by the reductant, that can act as heteroatom doping agent or provide additional crosslinking [35,36]. Because during self-assembly of rGOAs the rGO flakes behave like fishnet, the rGOA can be easily loaded with, e.g., metallic nanoparticles [64]. For example, the presence of alkaline metal cations bearing positive charge can enhance the interaction of the surface with benzene [65]. On the post-synthesis stage, the

rGOAs can be annealed in order to alter their physicochemical structure [66]. This brief overlook shows that there are different possibilities for tailoring rGOAs adsorbents.

#### 4. Conclusions

Reduced graphene oxide aerogels were successfully prepared by the reduction induced self-assembly with the aid of LAA, BS and DTN. With the use of benzene and cyclohexane, it was demonstrated that rGOAs can efficiently separate adsorbates in gas-phase adsorption processes. The adsorption performance was heavily dependent on a type of reductant. First time reported, DTN reduced aerogel (rGOA\_DTN), turned out to be the one with the uppermost adsorption capacity. For benzene, the single component breakthrough capacity was 1.3 and 6.8 times higher compared to rGOA\_BS and rGOA\_LAA, respectively, while for cyclohexane, it was 1.3 and 20.6 times higher. The adsorption capacity of aerogels positively correlated with the BET surface area. All aerogels were meso-macroporous adsorbents with the highest contribution of mesopores measured for rGOA\_DTN. Also, the pore size was the smallest for rGOA\_DTN, however, the adsorption capacity did not correlate with

the mesopores but with the macropores specific surface area. Thus, the different adsorption capacity for benzene and cyclohexane is caused by the different physicochemical structure of the surface of rGOAs. The IGC analysis revealed the impact of nanoroughness and  $\pi$ -conjugation on the adsorption of benzene and cyclohexane. In binary component, breakthrough experiment rGOA\_DTN demonstrated the selectivity of 2.09 and excellent thermal stability. With a simple heat treatment, it was reused multiple times without deterioration of the adsorption capacity and selectivity. This work indicates the potential for the development of adsorbents based on rGOAs for challenging gas-phase hydrocarbons separations.

### CRedit authorship contribution statement

**Maksymilian Plata-Gryl:** Conceptualization, Methodology, Investigation, Resources, Writing – original draft, Visualization, Project administration, Funding acquisition, Data curation. **Roberto Castro-Muñoz:** Writing – review & editing, Visualization, Supervision, Methodology. **Emilia Gontarek-Castro:** Writing – review & editing, Methodology, Investigation. **Alan Miralrio:** Writing – review & editing, Formal analysis. **Grzegorz Boczkaj:** Writing – review & editing, Visualization, Supervision, Resources, Methodology, Conceptualization.

### Declaration of competing interest

The authors declare that they have no known competing financial interests or personal relationships that could have appeared to influence the work reported in this paper.

### Data availability

The data that support the findings of this study are available in the Zenodo and Bridge of Knowledge open data repositories. DOI: 10.5281/zenodo.10912140

### Acknowledgements

Maksymilian Plata Gryl gratefully acknowledges the financial support from the National Science Centre, Cracow, Poland – Project PRELUDIUM18, no. UMO-2019/35/N/ST8/04226.

Prof. Grzegorz Boczkaj gratefully acknowledges financial support from the National Science Centre, Warsaw, Poland for project OPUS nr UMO-2021/41/B/ST8/01575.

### Appendix A. Supplementary data

Supplementary data to this article can be found online at <https://doi.org/10.1016/j.cej.2024.152782>.

### References

- [1] S. Mukherjee, D. Sensharma, O.T. Qazvini, S. Dutta, L.K. Macreadie, S.K. Ghosh, R. Babarao, Advances in adsorptive separation of benzene and cyclohexane by metal-organic framework adsorbents, *Coord. Chem. Rev.* 437 (2021) 213852, <https://doi.org/10.1016/j.ccr.2021.213852>.
- [2] F. Xie, L. Chen, E.M. Cedeño Morales, S. Ullah, Y. Fu, T. Thonhauser, K. Tan, Z. Bao, J. Li, Complete separation of benzene-cyclohexene-cyclohexane mixtures via temperature-dependent molecular sieving by a flexible chain-like coordination polymer, *Nat. Commun.* 15 (2024) 2240, <https://doi.org/10.1038/s41467-024-46556-6>.
- [3] A. Sekar, G.K. Varghese, M.K. Ravi Varma, Analysis of benzene air quality standards, monitoring methods and concentrations in indoor and outdoor environment, *Heliyon* 5 (2019) e02918.
- [4] M. Ayuso, A. Cañada-Barcala, M. Larriba, P. Navarro, N. Delgado-Mellado, J. García, F. Rodríguez, Enhanced separation of benzene and cyclohexane by homogeneous extractive distillation using ionic liquids as entrainers, *Sep. Purif. Technol.* 240 (2020) 116583, <https://doi.org/10.1016/j.seppur.2020.116583>.
- [5] X. Wang, H. Xu, Y. Zou, W. Hu, L. Wang, Mechanistic insight into separation of benzene and cyclohexane by extractive distillation using deep eutectic solvent as entrainer, *J. Mol. Liq.* 368 (2022) 120780, <https://doi.org/10.1016/j.molliq.2022.120780>.
- [6] G. Liu, W. Jin, Pervaporation membrane materials: Recent trends and perspectives, *J. Membr. Sci.* 636 (2021) 119557, <https://doi.org/10.1016/j.memsci.2021.119557>.
- [7] B.E. Poling, J.M. Prausnitz, J.P. O'Connell, *Properties of gases and liquids*, 5th Edition, McGraw-Hill Education, New York, 2001 <https://www.accessengineeringlibrary.com/content/book/9780070116825>.
- [8] D.W. Green, R.H. Perry, *Perry's chemical engineers' handbook*, Eighth Edition, 8th ed., McGraw-Hill Education, New York, 2008.
- [9] CRC Handbook of Chemistry and Physics, 84th Edition Edited by David R. Lide (National Institute of Standards and Technology). CRC Press LLC: Boca Raton. 2003. 2616 pp. \$139.95. ISBN 0-8493-0484-9., *J. Am. Chem. Soc.* 126 (2004) 1586–1586. Doi: 10.1021/ja0336372.
- [10] M.J. Emparan-Legaspi, J. Gonzalez, G. Gonzalez-Carrillo, S.G. Ceballos-Magaña, J. Canales-Vazquez, I.A. Aguayo-Villarreal, R. Muñoz-Valencia, Dynamic adsorption separation of benzene/cyclohexane mixtures on micro-mesoporous silica SBA-2, *Microporous Mesoporous Mater.* 294 (2020) 109942, <https://doi.org/10.1016/j.micromeso.2019.109942>.
- [11] G. Wang, B. Dou, Z. Zhang, J. Wang, H. Liu, Z. Hao, Adsorption of benzene, cyclohexane and hexane on ordered mesoporous carbon, *J. Environ. Sci.* 30 (2015) 65–73, <https://doi.org/10.1016/j.jes.2014.10.015>.
- [12] A. Valencia, R. Muñoz-Valencia, S.G. Ceballos-Magaña, C.K. Rojas-Mayorga, A. Bonilla-Petriciolet, J. González, I.A. Aguayo-Villarreal, Cyclohexane and benzene separation by fixed-bed adsorption on activated carbons prepared from coconut shell, *Environ. Technol. Innov.* 25 (2022) 102076, <https://doi.org/10.1016/j.eti.2021.102076>.
- [13] Y. Han, Y. Chen, Y. Ma, J. Bailey, Z. Wang, D. Lee, A.M. Sheveleva, F. Tuna, E.J. L. McInnes, M.D. Frogley, S.J. Day, S.P. Thompson, B.F. Spencer, M. Nikiel, P. Manuel, D. Crawshaw, M. Schröder, S. Yang, Control of the pore chemistry in metal-organic frameworks for efficient adsorption of benzene and separation of benzene/cyclohexane, *Chem* 9 (2023) 739–754, <https://doi.org/10.1016/j.chempr.2023.02.002>.
- [14] L.K. Macreadie, O.T. Qazvini, R. Babarao, Reversing benzene/cyclohexane selectivity through varying supramolecular interactions using aliphatic, isoreticular MOFs, *ACS Appl. Mater. Interfaces* 13 (2021) 30885–30890, <https://doi.org/10.1021/acsami.1c08823>.
- [15] A.A. Sapiyanik, K.A. Kovalenko, D.G. Samsonenko, M.O. Barsukova, D.N. Dybtsev, V.P. Fedin, Exceptionally effective benzene/cyclohexane separation using a nitro-decorated metal-organic framework, *Chem. Commun.* 56 (2020) 8241–8244, <https://doi.org/10.1039/D0CC03227A>.
- [16] Y. Ding, L.O. Alimi, B. Moosa, C. Maaliki, J. Jacquemin, F. Huang, N.M. Khashab, Selective adsorptive separation of cyclohexane over benzene using thienothiophene cages, *Chem. Sci.* 12 (2021) 5315–5318, <https://doi.org/10.1039/D1SC00440A>.
- [17] P.-F. Cui, X.-R. Liu, Y.-J. Lin, Z.-H. Li, G.-X. Jin, Highly selective separation of benzene and cyclohexane in a spatially confined carborane metallacage, *J. Am. Chem. Soc.* 144 (2022) 6558–6565, <https://doi.org/10.1021/jacs.2c01668>.
- [18] M. Jirásek, M. Rickhaus, L. Tejerina, H.L. Anderson, Experimental and theoretical evidence for aromatic stabilization energy in large macrocycles, *J. Am. Chem. Soc.* 143 (2021) 2403–2412, <https://doi.org/10.1021/jacs.0c12845>.
- [19] T. Sugahara, D. Hashizume, N. Tokitoh, H. Matsui, R. Kishi, M. Nakano, T. Sasamori, Characterization of resonance structures in aromatic rings of benzene and its heavier-element analogues, *Phys. Chem. Chem. Phys.* 24 (2022) 22557–22561, <https://doi.org/10.1039/D2CP03068C>.
- [20] N. Kumar, A.S. Gaur, G.N. Sastry, A perspective on the nature of cation- $\pi$  interactions, *J. Chem. Sci.* 133 (2021) 97, <https://doi.org/10.1007/s12039-021-01959-6>.
- [21] R.M. del Castillo, A. Miralrio, C. Rios, R. Salcedo, Organometallic complexes of carbon nanotori, *J. Mol. Model.* 25 (2019) 239, <https://doi.org/10.1007/s00894-019-4118-0>.
- [22] C. González-Galán, A. Luna-Triguero, J.M. Vicent-Luna, A.P. Zaderenko, A. Ślawek, R. Sánchez-de-Armas, S. Calero, Exploiting the  $\pi$ -bonding for the separation of benzene and cyclohexane in zeolites, *Chem. Eng. J.* 398 (2020) 125678, <https://doi.org/10.1016/j.cej.2020.125678>.
- [23] H. Yao, Y.-M. Wang, M. Quan, M.U. Farooq, L.-P. Yang, W. Jiang, Adsorptive separation of benzene, cyclohexene, and cyclohexane by amorphous nonporous amide naphthotube solids, *Angew. Chem.* 132 (2020) 20117–20122, <https://doi.org/10.1002/ange.202009436>.
- [24] G. Deng, Z. Wang, Triptycene-based microporous cyanate resins for adsorption/separations of benzene/cyclohexane and carbon dioxide gas, *ACS Appl. Mater. Interfaces* 9 (2017) 41618–41627, <https://doi.org/10.1021/acsami.7b15050>.
- [25] H. Tan, Q. Chen, T. Chen, H. Liu, Selective adsorption and separation of Xylene isomers and benzene/cyclohexane with microporous organic polymers POP-1, *ACS Appl. Mater. Interfaces* 10 (2018) 32717–32725, <https://doi.org/10.1021/acsami.8b11657>.
- [26] M. Moroni, E. Roldan-Molina, R. Vismara, S. Galli, J.A.R. Navarro, Impact of pore flexibility in imine-linked covalent organic frameworks on benzene and cyclohexane adsorption, *ACS Appl. Mater. Interfaces* 14 (2022) 40890–40901, <https://doi.org/10.1021/acsami.2c09911>.
- [27] C. Jansen, N. Assahub, A. Spieß, J. Liang, A. Schmitz, S. Xing, S. Gökpınar, C. Janiak, The complexity of comparative adsorption of C6 hydrocarbons (Benzene, Cyclohexane, n-Hexane) at metal-organic frameworks, *Nanomaterials* 12 (2022) 3614, <https://doi.org/10.3390/nano12203614>.
- [28] M. Plata-Gryl, M. Momotko, S. Makowicz, G. Boczkaj, Characterization of diatomaceous earth coated with nitrated asphaltene as superior adsorbent for

- removal of VOCs from gas phase in fixed bed column, *Chem. Eng. J.* 427 (2022) 130653, <https://doi.org/10.1016/j.cej.2021.130653>.
- [29] M. Plata-Gryl, M. Momotko, S. Makowiec, G. Boczkaj, Highly effective asphaltene-derived adsorbents for gas phase removal of volatile organic compounds, *Sep. Purif. Technol.* 224 (2019) 315–321, <https://doi.org/10.1016/j.seppur.2019.05.041>.
- [30] J. Cai, J. Tian, H. Gu, Z. Guo, Amino carbon nanotube modified reduced graphene oxide aerogel for oil/water separation, *ES Mater. Manuf.* 6 (2019) 68–74, <https://doi.org/10.30919/esmm5f611>.
- [31] T.T.P.N.X. Trinh, D.M. Nguyet, T.H. Quan, T.N.M. Anh, D.B. Thinh, L.T. Tai, N. T. Lan, D.N. Trinh, N.M. Dat, H.M. Nam, M.T. Phong, N.H. Hieu, Preparing three-dimensional graphene aerogels by chemical reducing method: Investigation of synthesis condition and optimization of adsorption capacity of organic dye, *Surf. Interfaces* 23 (2021) 101023, <https://doi.org/10.1016/j.surfin.2021.101023>.
- [32] H. Gao, S. Chen, S. Wei, W. Li, M. Zhang, N. Sun, Facile synthesis of ultralight S-doped Co 3 O 4 microflowers@reduced graphene oxide aerogels with defect and interface engineering for broadband electromagnetic wave absorption, *J. Mater. Chem. C* 10 (2022) 12630–12643, <https://doi.org/10.1039/D2TC02356C>.
- [33] K. Fu, J. Zhao, F. Liu, L. Wu, Z. Jin, Y. Yang, J. Qiao, Z. Wang, F. Wang, J. Liu, Enhanced electromagnetic wave absorption of nitrogen-doped reduced graphene oxide aerogels with LaFeO<sub>3</sub> cluster modifications, *Carbon* 210 (2023) 118071, <https://doi.org/10.1016/j.carbon.2023.118071>.
- [34] Y.M.Y. Albarqouni, S.P. Lee, G.A.M. Ali, A.S. Ethiraj, H. Algarni, K.F. Chong, Facile synthesis of reduced graphene oxide aerogel in soft drink as supercapacitor electrode, *J. Nanostructure Chem.* 12 (2022) 417–427, <https://doi.org/10.1007/s40097-021-00424-7>.
- [35] M.S. Çögenli, A. Bayrakçeken Yurtcan, Heteroatom doped 3D graphene aerogel supported catalysts for formic acid and methanol oxidation, *Int. J. Hydrog. Energy* 45 (2020) 650–666, <https://doi.org/10.1016/j.ijhydene.2019.10.226>.
- [36] D. Zhao, Y. Wang, S. Zhao, M. Wakeel, Z. Wang, R.S. Shaikh, T. Hayat, C. Chen, A simple method for preparing ultra-light graphene aerogel for rapid removal of U (VI) from aqueous solution, *Environ. Pollut.* 251 (2019) 547–554, <https://doi.org/10.1016/j.envpol.2019.05.011>.
- [37] J. Kaushik, C. Sharma, N.K. Lamba, P. Sharma, G.S. Das, K.M. Tripathi, R.K. Joshi, S.K. Sonkar, 3D porous MoS<sub>2</sub>-decorated reduced graphene oxide aerogel as a heterogeneous catalyst for reductive transformation reactions, *Langmuir* 39 (2023) 12865–12877, <https://doi.org/10.1021/acs.langmuir.3c01785>.
- [38] Q. Li, D. Chen, J. Miao, S. Lin, Z. Yu, Y. Han, Z. Yang, X. Zhi, D. Cui, Z. An, Ag-modified 3D reduced graphene oxide aerogel-based sensor with an embedded microheater for a fast response and high-sensitive detection of NO<sub>2</sub>, *ACS Appl. Mater. Interfaces* 12 (2020) 25243–25252, <https://doi.org/10.1021/acsami.9b22098>.
- [39] J. Li, X. Li, X. Zhang, J. Zhang, Y. Duan, X. Li, D. Jiang, T. Kozawa, M. Naito, Development of graphene aerogels with high strength and ultrahigh adsorption capacity for gas purification, *Mater. Des.* 208 (2021) 109903, <https://doi.org/10.1016/j.matdes.2021.109903>.
- [40] C. Gao, Z. Dong, X. Hao, Y. Yao, S. Guo, Preparation of reduced graphene oxide aerogel and its adsorption for Pb(II), *ACS Omega* 5 (2020) 9903–9911, <https://doi.org/10.1021/acsomega.0c00183>.
- [41] X. Hou, Y. Zheng, X. Ma, Y. Liu, Z. Ma, The effects of hydrophobicity and textural properties on hexamethyldisiloxane adsorption in reduced graphene oxide aerogels, *Molecules* 26 (2021) 1130, <https://doi.org/10.3390/molecules26041130>.
- [42] D. Guo, P. Cai, J. Sun, W. He, X. Wu, T. Zhang, X. Wang, X. Zhang, Reduced-graphene-oxide/metal-oxide p-n heterojunction aerogels as efficient 3D sensing frameworks for phenol detection, *Carbon* 99 (2016) 571–578, <https://doi.org/10.1016/j.carbon.2015.12.074>.
- [43] A. Memetova, I. Tyagi, P. Singh, E. Neskoromnaya, R.R. Karri, A. Zelenin, N. Memetov, A. Babkin, R. Stolyarov, N. Chapaksov, A. Gusev, N.M. Mubarak, A. Tkachev, Suhas, Reduced graphene oxide based composite aerogels for energy storage and transportation of methane, *J. Clean. Prod.* 379 (2022) 134770, <https://doi.org/10.1016/j.jclepro.2022.134770>.
- [44] P. Xia, Z. Zhang, Z. Tang, Y. Xue, J. Li, G. Yang, Preparation and electrochemical performance of three-dimensional vertically aligned graphene by unidirectional freezing method, *Molecules* 27 (2022) 376, <https://doi.org/10.3390/molecules27020376>.
- [45] M. Plata-Gryl, R. Castro-Muñoz, G. Boczkaj, Chemically reduced graphene oxide based aerogels - Insight on the surface and textural functionalities dependent on handling the synthesis factors, *Colloids Surf. Physicochem. Eng. Asp.* 675 (2023) 132005, <https://doi.org/10.1016/j.colsurfa.2023.132005>.
- [46] J. Zhan, Z. Lei, Y. Zhang, Non-covalent interactions of graphene surface: Mechanisms and applications, *Chem* 8 (2022) 947–979, <https://doi.org/10.1016/j.chempr.2021.12.015>.
- [47] D.C. Marcano, D.V. Kosynkin, J.M. Berlin, A. Sinitskii, Z. Sun, A. Slesarev, L. B. Alemany, W. Lu, J.M. Tour, Improved synthesis of graphene oxide, *ACS Nano* 4 (2010) 4806–4814, <https://doi.org/10.1021/nn1006368>.
- [48] J.P. Perdew, K. Burke, M. Ernzerhof, Generalized gradient approximation made simple, *Phys. Rev. Lett.* 77 (1996) 3865–3868, <https://doi.org/10.1103/PhysRevLett.77.3865>.
- [49] F. Weigend, R. Ahlrichs, Balanced basis sets of split valence, triple zeta valence and quadruple zeta valence quality for H to Rn: Design and assessment of accuracy, *Phys. Chem. Chem. Phys.* 7 (2005) 3297, <https://doi.org/10.1039/b508541a>.
- [50] S. Grimme, S. Ehrlich, L. Goerigk, Effect of the damping function in dispersion corrected density functional theory, *J. Comput. Chem.* 32 (2011) 1456–1465, <https://doi.org/10.1002/jcc.21759>.
- [51] S.G. Balasubramani, G.P. Chen, S. Coriani, M. Diefenbach, M.S. Frank, Y. J. Franzke, F. Furch, R. Grotjahn, M.E. Harding, C. Hättig, A. Hellweg, B. Helmich-Paris, C. Holzer, U. Huniar, M. Kaupp, A. Marefat Khah, S. Karbalaee Khani, T. Müller, F. Mack, B.D. Nguyen, S.M. Parker, E. Perlt, D. Rappoport, K. Reiter, S. Roy, M. Rückert, G. Schmitz, M. Sierka, E. Tapavicz, D.P. Tew, C. van Willen, V.K. Voora, F. Weigend, A. Wodyński, J.M. Yu, Turbomole, Modular program suite for ab initio quantum-chemical and condensed-matter simulations, *J. Chem. Phys.* 152 (2020) 184107, <https://doi.org/10.1063/5.0004635>.
- [52] M.D. Hanwell, D.E. Curtis, D.C. Lonie, T. Vandermeersch, E. Zurek, G.R. Hutchison, Avogadro: an advanced semantic chemical editor, visualization, and analysis platform, *J. Cheminformatics* 4 (2012) 17, <https://doi.org/10.1186/1758-2946-4-17>.
- [53] X. Zhang, Z. Sui, B. Xu, S. Yue, Y. Luo, W. Zhan, B. Liu, Mechanically strong and highly conductive graphene aerogel and its use as electrodes for electrochemical power sources, *J. Mater. Chem.* 21 (2011) 6494–6497, <https://doi.org/10.1039/C1JM10239G>.
- [54] M. Thommes, Physical adsorption characterization of nanoporous materials, *Chem. Ing. Tech.* 82 (2010) 1059–1073, <https://doi.org/10.1002/cite.201000064>.
- [55] D. Zhi, T. Li, J. Li, H. Ren, F. Meng, A review of three-dimensional graphene-based aerogels: Synthesis, structure and application for microwave absorption, *Compos. Part B Eng.* 211 (2021) 108642, <https://doi.org/10.1016/j.compositesb.2021.108642>.
- [56] K.S.W. Sing, R.T. Williams, Physisorption hysteresis loops and the characterization of nanoporous materials, *Adsorpt. Sci. Technol.* 22 (2004) 773–782, <https://doi.org/10.1260/0263617053499032>.
- [57] J. Aihara, Reduced HOMO–LUMO gap as an index of kinetic stability for polycyclic aromatic hydrocarbons, *J. Phys. Chem. A* 103 (1999) 7487–7495, <https://doi.org/10.1021/jp990992i>.
- [58] M.O. Sinnokrot, E.F. Valeev, C.D. Sherrill, Estimates of the Ab initio limit for  $\pi$ – $\pi$  interactions: The benzene dimer, *J. Am. Chem. Soc.* 124 (2002) 10887–10893, <https://doi.org/10.1021/ja025896h>.
- [59] Y. Shen, X. Zhu, B. Chen, Size effects of graphene oxide nanosheets on the construction of three-dimensional graphene-based macrostructures as adsorbents, *J. Mater. Chem. A* 4 (2016) 12106–12118, <https://doi.org/10.1039/C6TA04112D>.
- [60] K. Zhang, R.P. Lively, C. Zhang, R.R. Chance, W.J. Koros, D.S. Sholl, S. Nair, Exploring the framework hydrophobicity and flexibility of ZIF-8: From biofuel recovery to hydrocarbon separations, *J. Phys. Chem. Lett.* 4 (2013) 3618–3622, <https://doi.org/10.1021/jz402019d>.
- [61] B. Dou, Q. Hu, J. Li, S. Qiao, Z. Hao, Adsorption performance of VOCs in ordered mesoporous silicas with different pore structures and surface chemistry, *J. Hazard. Mater.* 186 (2011) 1615–1624, <https://doi.org/10.1016/j.jhazmat.2010.12.051>.
- [62] J. Yan, H. Sun, Q. Wang, L. Lu, B. Zhang, Z. Wang, S. Guo, F. Han, Covalent triazine frameworks for the dynamic adsorption/separation of benzene/cyclohexane mixtures, *New J. Chem.* 46 (2022) 7580–7587, <https://doi.org/10.1039/D2NJ00727D>.
- [63] S. Shi, S. Ren, S. Hao, Y. Chen, C. Yang, S. Dai, Graphene aerogel induced by ethanol-assisted method for excellent electromagnetic wave absorption, *J. Mater. Sci.* 57 (2022) 453–466, <https://doi.org/10.1007/s10853-021-06461-5>.
- [64] J. Liang, Y. Ling, X. Wu, H.A. Acciari, Z. Zhang, Fishnet-like Ni–Fe–N co-modified graphene aerogel catalyst for highly efficient oxygen reduction reaction in an alkaline medium, *J. Appl. Electrochem.* 49 (2019) 1211–1226, <https://doi.org/10.1007/s10800-019-01360-9>.
- [65] I. Soteras, M. Orozco, F.J. Luque, Induction effects in metal cation–benzene complexes, *Phys. Chem. Chem. Phys.* 10 (2008) 2616–2624, <https://doi.org/10.1039/B719461G>.
- [66] M. Zeeshan, K. Yalcin, F.E. Sarac Oztuna, U. Unal, S. Keskin, A. Uzun, A new class of porous materials for efficient CO<sub>2</sub> separation: Ionic liquid/graphene aerogel composites, *Carbon* 171 (2021) 79–87, <https://doi.org/10.1016/j.carbon.2020.08.079>.